ISO observations of a sample of CSS/GPS sources

C. Fanti, F. Pozzi
Istituto di Radioastronomia, CNR, Bologna

IRA 235/97

Compact Steep Spectrum (CSS) and GHz Peaked spectrum (GPS) radio sources are powerful extragalactic radio sources with radio emission which is confined well within the host galaxies. They are thought to be either young objects, which have yet to develop extended radio lobes, or sources where the radio emitting plasma is trapped by an unusually dense interstellar medium. The medium will likely have a substantial cold phase and a large amount of dust. This dust will absorb and reprocess a high fraction of the optical and UV radiation from the AGN making CSS/GPS strong IR sources. Since the dense medium, responsible for trapping the radio sources, has to extend over several kpc from the nucleus, the dust will be cold so that the IR emission is expected especially in the medium-far IR (MFIR) spectral region.

Comparing MFIR emission from a sample of CSS/GPS with that of a sample of extended objects, it is possible to determine which of the two scenarios is correct.

ISO is the only instrument, at present, capable of producing detections of the MFIR emission of CSS/GPS radio sources and comparison samples.

Summary. This is a progress report on the data analysis of about 80% of the CSS/GPS and reference sample sources selected for observations with ISOPHOT at $\lambda = 60, 90, 160, 200\mu$m. A few $\lambda = 11.5\mu$m are also available, but have not been analized yet. We do not describe here the instrument nor the way to derive from the actual photon counts the source flux. For this we refere to the ISO and PIA manuals. We shall describe the way in which the observations have been performed and the accurate (as far as possible) data reduction. The signal we are trying to detect is very weak in comparison with the Galaxy background, therefore the noise has to be pushed down as much as possible. We found that effects like *vignetting* and *flat fielding* may be important in our case.

No individual detections have been found except for 1345+125, which, however, has a Seyfert nucleus, and is not, therefore, a typical CSS. A few "suspect" detections, among both CSS/GPS and reference sources, are mentioned. The co–addition of all the observations possibly provides average fluxes at 60, 90 and 160μm, but for the 200μm reduction problems do not allow us to use the found average value.

Our analysis proves that the 90μm detector, in spite of ISOPHOT not performing as originally planned, is by far superior to IRAS. At 60μm the two instruments seem, at the moment, comparable, but we must consider that ISO is not yet well understood, and that the data analysis still needs to be improved. We hope that much better data will become available in the future.

From the average source emission we conclude that there is no difference between CSS/GPS and reference sources. Moreover we can derive the temperature of the dust radiating in this frequency range ($T = 44 \pm 2$K) and its mass ($(2.3 \pm 0.5) \times 10^6 M_\odot$). Assuming typical gas/dust mass ratios we find that the inferred gas mass is one to two order of magnitude less than required to frustrate CSS/GPS sources.

1 Observations

The sample actually scheduled for observations (table 1) is slighty different from the original one, due to the overheads being longer than originally estimated. This turned out in a reduction of the number of observable sources.

Some other source, mainly among the reference sources, belonged to other experiments, and we had to bargain with other collegues. The major time cut occurred for 11.5μm, but we kept, as far as possible, those objects for which KNO observations existed or were in progress (marked with a † in table 1).

In the table log $P_{2.7}$ is computed with H_0=100 and q_0=0.5. ION is the *Iso Observing Number*. Sources with an * are those analysed so far and discussed in this report.

The sources were observed with ISOPHOT, sub–instruments C100 & C200 at the wavelengths of 60, 90, 160 & 200 μm. Since some of our sources were planned by GTO's (Guarantee Time Observations) at some of our selected wavelengths, especially 60, 90 & 160 μm, we were not allowed to repeat those observations, therefore not all sources have been observed by us at all four frequencies (see tables 11–16).

CSS

Source	log $P_{2.7}$ W/Hz	z	ION	Source	log $P_{2.7}$ W/Hz	z	ION
3C49*	26.89	0.62	7	3C318*	27.01	0.75	32
3C67†	26.30	0.31	9	1607+26†*	26.92	0.47	34
0404+76†	27.23	0.6	12	3C343.1*	27.24	0.75	41
1031+56	26.64	0.46	15	1819+39†*	26.9	0.6	48
3C268.3†*	26.54	0.37	17	1819+6707*	25.06	0.22	50
1323+321*	26.75	0.37	22	1829+29*	26.96	0.6	52
1345+125*	25.79	0.12	24	1934-63†*	26.65	0.18	56
1358+624†*	26.81	0.43	26	2342+82*	27.25	0.74	61
3C303.1†*	25.60	0.27	30	2352+49†*	26.18	0.24	63

Reference Sources

Source	log $P_{2.7}$ W/Hz	z	ION	Source	log $P_{2.7}$ W/Hz	z	ION
3C16*	26.31	0.41	1	3C284*	25.87	0.24	21
3C19*	26.77	0.48	2	3C295*	26.51	0.46	28
3C34*	26.67	0.69	3	3C299*	26.44	0.37	29
3C42*	26.51	0.40	5	3C330*	27.18	0.55	36
3C46*	26.18	0.44	6	3C337*	26.96	0.64	37
3C79*	26.32	0.26	11	3C401*	26.12	0.20	58
3C220.1	26.87	0.61	14	3C441*	27.03	0.71	59
3C274.1*	26.52	0.42	19	3C459*	26.18	0.22	60
3C277.2	26.92	0.77	20				

Table 1: The sample

filter μm	d_{Airy} ["]	f_{PSF}	filter	d_{Airy} ["]	f_{PSF}
C100			**C200**		
60	50.3	0.69	160	134	0.64
90	75.5	0.61	200	168	0.59

Table 2: Airy disk size, d_{Airy} and f_{PSF} for the filters used by us

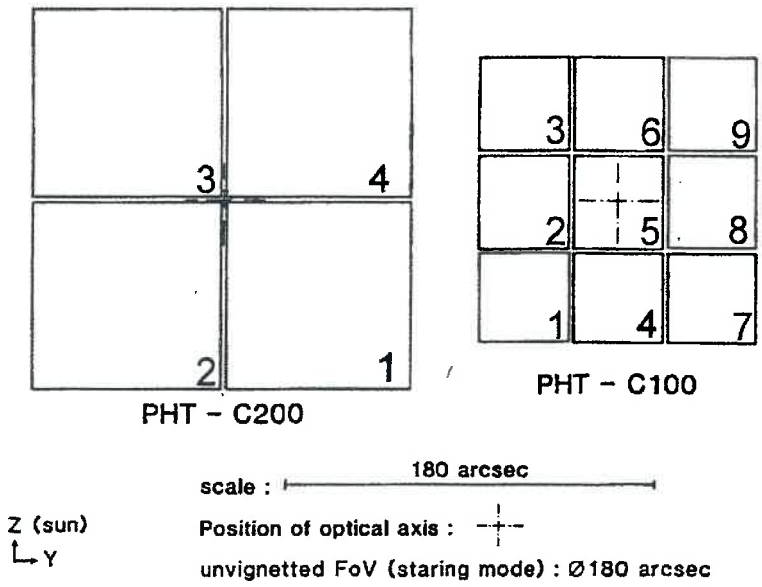

Figure 1: C100 and C200 detectors. Pixel sizes are $43.5'' \times 43.5''$ for C100 and $89.4'' \times 89.4''$ for C200

In order to remove the background, the observations were performed in *chopper* rectangular mode, with chopper through 180", in order to have, every few seconds, (*chopper plateau*) an ON–source and an OFF–source measure. We shall then subtract OFF from ON data, in order to extract the signal (ON–OFF). With this observing mode, the telescope points halfway between the source and the background positions, and a little movable mirror switches between the two sky positions. This introduces a vignetting error which is different for ON and OFF positions (see sect. 2).

We recall that C100 and C200 detectors provide 3×3 and 2×2 pixel matrices (fig.1). Each pixel is an independent detector, which requires its own calibration.

The size of the Airy disk of the Point Spread Function (PSF) and f_{PSF}, the fraction of light falling onto one pixel (for a source at the pixel center) are given in table 2. By comparison with fig. 1 it is clear that for C100 the Airy disk hardly matches one pixel size while for C200 the PFS covers most of the matrix. Therefore detected sources will be visible mostly on the central pixel #5 with C100, while with C200 the four pixels should give the same values (within the noise). This is shown by the *lego plots* in figures 2 and 3. Note that in fig. 3 the four pixels do not have the same height: this is due to the not yet corrected vignetting error (see sect. 2).

In the next sections we use the unit *mJy/pixel* to refer to the flux falling onto *one single* pixel. The source flux should be measured by fitting a PSF of known size to the ON–OFF matrix values. In practice, for C200 the flux is obtained by summing the four matrix pixels; for C100, since our signal is always very weak and will eventually affect only pixel #5, everytime this is required we convert mJy/pixel to mJy by simply dividing the flux falling onto pixel #5 by the value of f_{PSF} given in table 2

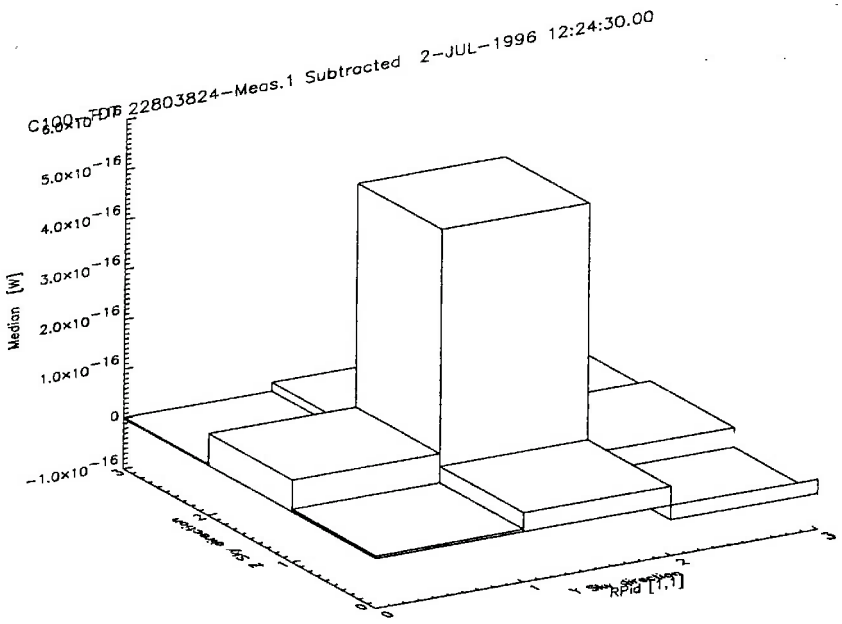

Figure 2: *lego plot* for C100

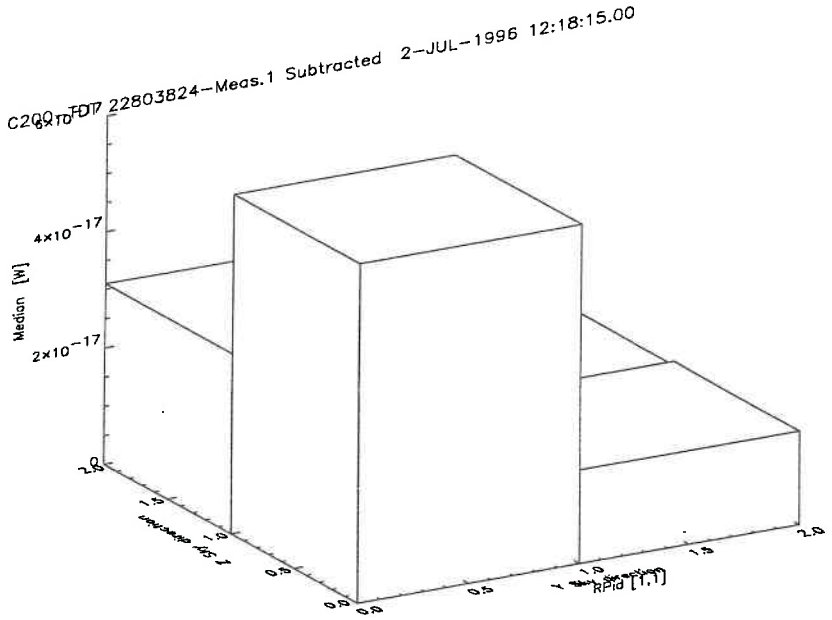

Figure 3: *lego plot* for C200

2 Data reduction

The data sent by the ISO reduction center were not scientifically validated yet, so we had to make the complete data reduction ourselves, starting from the ERD (**E***dit* **R***aw* **D***ata*) data. We used the PIA V6.1 (*Iso***p***hot* **I***nteractive* **A***nalisis*) software made available by the Heidelberg group.

This software removes glitches due to cosmic rays, subtracts the dark current, corrects for some kind of drits, derives the signals from the *ramps*, performs ON–OFF subraction and calibrates the data. It does **not** correct yet for vignetting, flat fielding, memory effects in the electronics, and any other error of which we (they) are not aware at the moment.

This is why this data reduction can only be considered preliminary. The results, however, are already interesting (setc. 4)

2.1 Calibration

The conversion from *volt/sec* into *watt* is made by using an internal calibration source (*lamp*) which gives the conversion values for each of the pixels in fig. 1. Then the conversion to *Jy* makes use of the instrument and filter characteristics, which are (or should be) known. The flux density scale is not final yet. It has been changing by factors of two in this year. Now rumors are that it is still 20% uncertain. This uncertainty is a minor problem for us. (see sec. 4)

2.2 Vignetting

In the future this correction will be performed by PIA, but we had to make it a–posteriori. Given the values of the background (see figures 5 and 6, and table 3), the corrections to apply are at most of a few % of the signal. This corresponds to errors of a few to a few tens of mJy/pixel. This is comparable or stronger than the signal we have (see tables 5 and 7).

Fortunately the way in which PIA subtracts the background in each chopper plateau is well explained in the manuals and we were able, with a little algebra, to apply the corrections provided to us by Martin Haas, of the Heidelberg group. The corrections are not very large (except for $\lambda = 160\mu$m) and we suspect that the corrections are not yet well established. The results are displayed in figure 4 where are reported, for each pixel, the source average of the original and of the corrected ON–OFF values. Clearly for 60 and 90 μm there is some improvement, especially on pixel #8. At 160 μm the correction is good for pixels 1,2,3, which are now fairly "flat", but at 200μm we do not believe the correction is right. This will be taken into proper account in section 4.

2.3 Nominal Noise

Nominal noise is computed with the equation

$$NEP_{tot} = \sqrt{NEP^2_{source} + 2NEP^2_{bck} + 2NEP^2_{rec}} \qquad (1)$$

where NEP's are the **N**oise **E**quivalent **P**ower of source, background and receiver (to be computed from ISO manuals) which depend on the ON–source time. The factors 2 in eq. 1 derive from the fact the the signal is obtained from ON–OFF measurements. From eq. 1 one obtains (see ISOPHOT manuals) the noise flux *in one pixel* (σ_n). From the values of the parameters

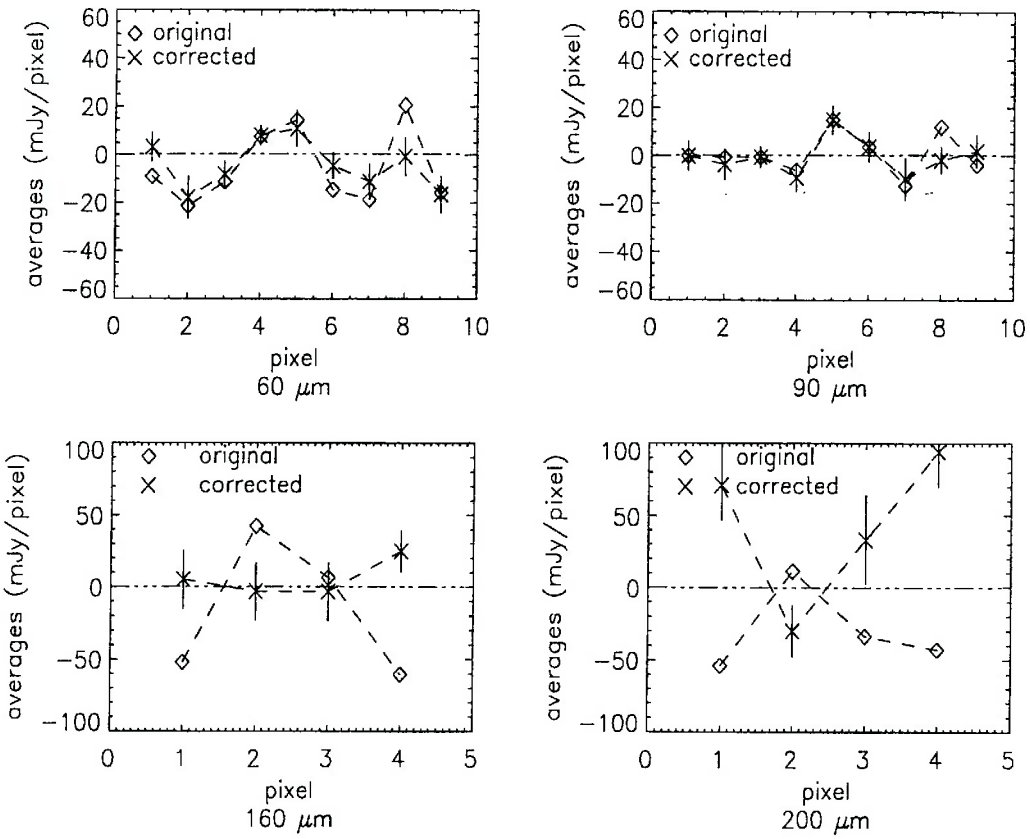

Figure 4: ON–OFF source average as a function of pixel #

necessary to compute the NEP's given in the manuals, it is clear that, except for very high backgrounds ($\gtrsim 20 - 30$ MJy/ster) or for very strong sources the receiver contribution to the nominal noise dominates. This is indeed our case. Typical values of (σ_n) in our observations are given in table 3, for different backgrounds and integration times.

To the nominal noise computed from eq. 1, *extragalactic source* and *cirrus* confusion have to be added. The latter depend only on the aperture/pixel size and on the sky position. Note that while galaxy confusion (*g.c.*) depends only on the observing wavelength (and on the galaxy evolution model) cirrus confusion (*c.c.*) strongly depends also on the background according to

$$c.c. \propto B^{1.5} \tag{2}$$

In order to see if any sources of our sample are detected, we need to carefully evaluate all these contribution. Actually, the best way to proceed is to adopt a pragmatical method, and try to estimate the noise from the data themselves. A possible approach could be to study the statistics of the background measurements. When allowance is made for (2) this statistics should include all possible noise effects.

2.4 Flat Fielding

We have studied *for each source* the r.m.s. (σ_b) distribution of the OFF (background) observations, corrected for vignetting (sect. 2.2). The results were:

1) the fluxes from pixel to pixel fluctuate much more than the nominal noise error (eq. 1)

2) the r.m.s. (σ_b) increases as a function of background much more than expected from eq. 1 (see figures 5 and 6)

In all figures 5–8 the ON–OFF r.m.s. (σ_s) values, are also plotted for comparison (pixel #5 excluded in C100). The lines are the least square weighted fits to the data points.

Points (1) and (2) are consistent with a calibration error different for each pixel of each detector. The correcting values are not available to us, therefore we have self–determined them from the data by computing for each pixel of each OFF–source measure the ratio

$$R_{ik} = \frac{p_{ik}^{off}}{< p_k^{off} >} \tag{3}$$

where p is the pixel value, k is the source index, i the pixel index and $< p_k^{off} >$ the average background, taken on the detector matrix, for the k-th source. We have adopted

$$f_i =< R_{ik} >_k \tag{4}$$

as calibration errors. The slopes of the straight lines in figures 5–6 are consistent with the r.m.s. of the f_i calibration factors of each detector: this confirms our hypothesis.

Figures 7 and 8 give the backgorund r.m.s after the application of this correction. The improvement is impressive but the background noise is still too high especially at the longest wavelengths. Infact, we would expect that σ_s, the r.m.s. on the ON–OFF measurements, be roughly $\sqrt{2} \times \sigma_b$, which is obviously not true.

We conclude therefore that the *determination of the noise from the background measurements is not reliable enough.*

2.4.1 Contribution of cyrrus confusion

Note that also the statistics of ON–OFF (σ_s) is peculiar at long wavelengths, since it keeps increasing with background much more than expected from eq. 1. Typical values for σ_s (taken over sub–samples of sources in comparable backgrounds) and σ_n are given in table 3, for different average backgrounds and integration times. The discrepancy between the two sets of values is striking.

A possible explanation could be galaxy and cirrus confusion. However, if we add to σ_n^2 $2 \times (\sigma_{g.c}^2$ and $\sigma_{c.c}^2)$ (the factor 2 is due to the ON–OFF measurements) we can roughly reproduce σ_s at 60 and 90 μm, but certainly not at 160 and 200 μm, at least at backgrounds $\gtrsim$ 10MJy/sr.

The values for $\sigma_{g.c}$ and $\sigma_{c.c}$ are derived by IRSKY software from IRAS data, and are quite certain at λ <100μm since in this range IRAS observations do exist, but are extrapolated by means of models at longer wavelengths. Therefore the discrepancy could be due to an uncertain knowledge of the model. But we are rather inclined to think that a large part of the disagreement derives from instrumental errors not properly corrected yet.

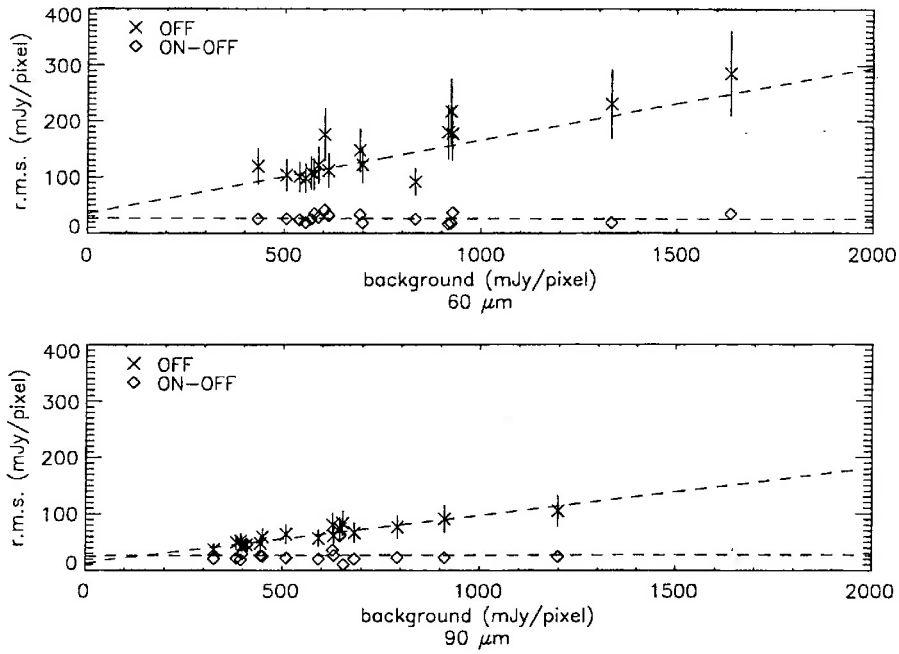

Figure 5: r.m.s for each source as a function of background. Crosses represent σ_b, diamonds σ_s (pixel #5 excluded)

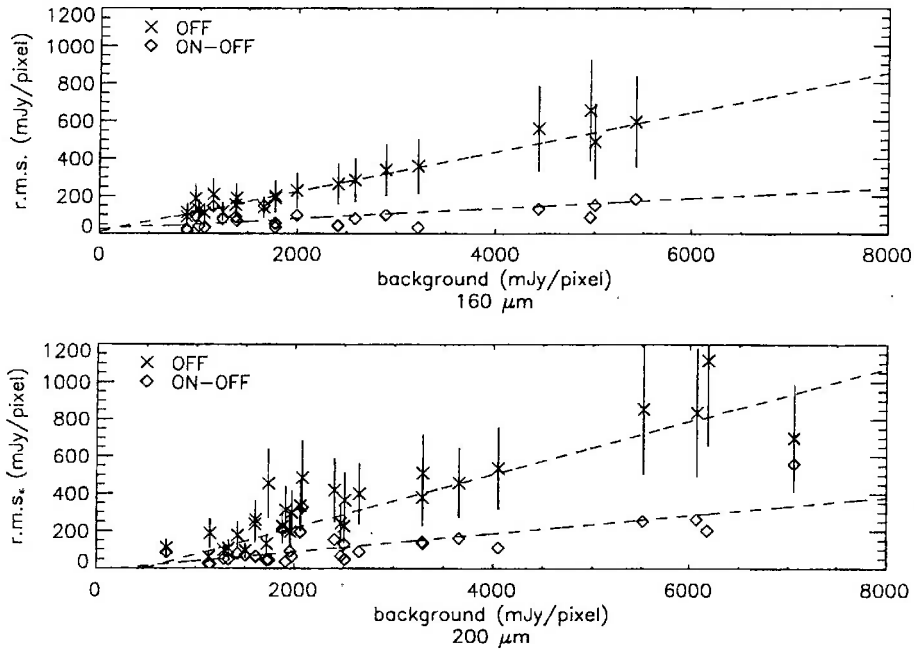

Figure 6: r.m.s for each source as a function of background. Crosses represent σ_b, diamonds σ_s

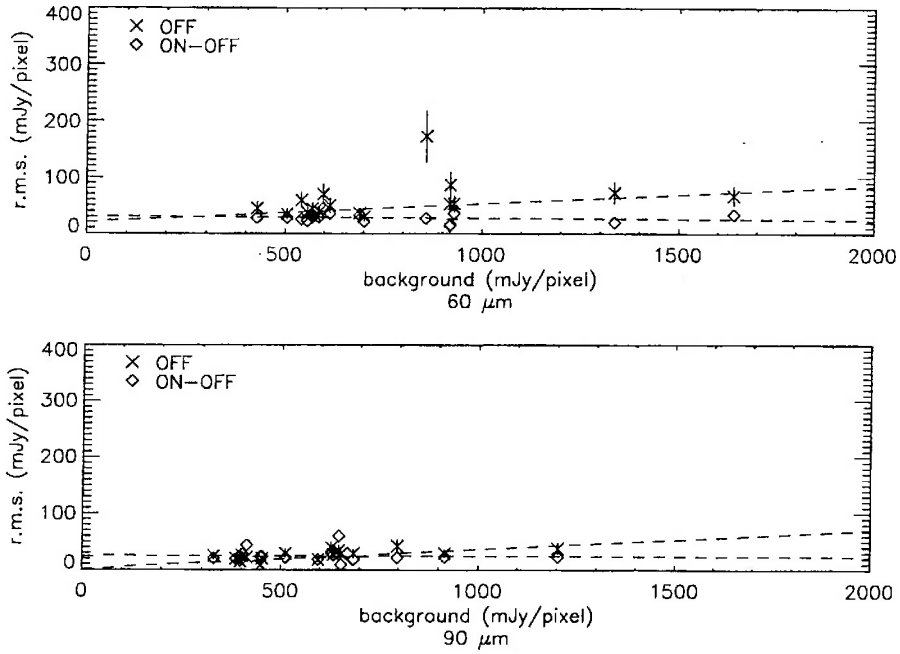

Figure 7: r.m.s for each source as a function of background after flat–fielding correction. Crosses represent σ_b, diamonds σ_s (pixel #5 excluded)

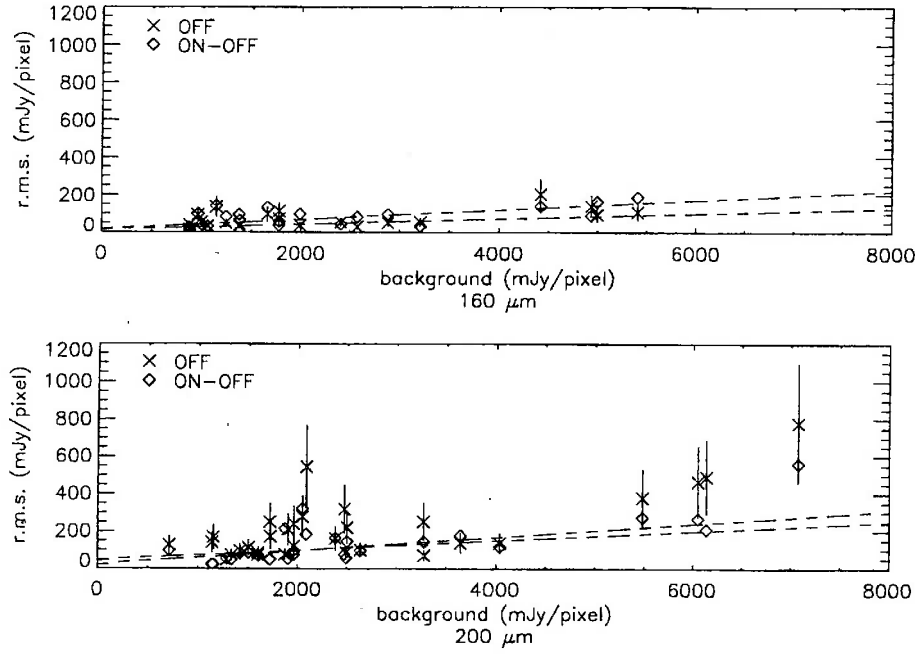

Figure 8: r.m.s for each source as a function of background after flat–fielding correction. Crosses represent σ_b, diamonds σ_s

λ μm	<bck.> MJy/sr	int.t s	σ_s mJy/pixel	σ_n mJy/pixel	$\sigma_{g.c}$ mJy/pixel	$\sigma_{c.c}$ mJy/pixel
60	≈ 13	64	29	17	2	13
90	≈ 11	32	25	11	4	22
160	≈ 6	32	79	27	22	8
	≈ 12	32	103	28		17
	≈ 26	64	163	104		60
200	≈ 6	32	58	100	23	3
	≈ 9	64	85	71		6
	≈ 10	32	156	100		7
	≈ 15	64	162	73		13
	≈ 30	128	312	54		36

Table 3: Typical r.m.s. of the ON–OFF measure [σ_s], of the nominal noise [σ_n] and of the extragalactic [$\sigma_{g.c}$] and cirrus [$\sigma_{c.c}$] confusion. The latter two are derived from IRAS data by IRSKY software. (The conversion from *mJy/pixel* to *MJy/sr* is obtained by dividing the flux in one pixel by the pixel area is steradian)

3 Data analysis

In tables 11–16 we give the actual values, corrected for vignetting and flat-fielding. For each source we give, for each pixel, on three different lines, the values (mJy/pixel) of the OFF–source (background), of the ON–source (background + source) and of the ON–OFF (source only) measurements. Note that the ON–OFF are slightly different from what one would compute by hand, due to the way (not described here) in which the PIA software computes this value. In the first column the source number is the one given in table 1. An R indicates a source from the reference sample.

3.1 Noise estimate

Since the background statistics is *not* (yet) a good noise estimator, we have adopted the following approach:

- for C100 we used the statistics of *all* ON–OFF measurements on *pixels other than* #5. With this method all the systematic errors should cancel (unless there are more errors, like vignetting, which are different for ON and OFF measurements). This approach is correct enough in our case, since, given the weakness of our objects, an eventual detection will affect only pixel #5 (sect. 1) while the other pixels will contain noise only.
- for C200 we can only compute source fluxes, by adding the four ON–OFF pixel values in each matrix, and then study the *flux statistics*. We are aware that this will give us upper limits to the noise, since it may include some true signal, weaker than or comparable to the noise itself.

For C100 the noise is rather well behaved (figures 9 and 10)) and gaussian. Its r.m.s. value (σ_T) (computed with exclusion of source #24, clearly detected, see sect. 3.2) is given in table 5.

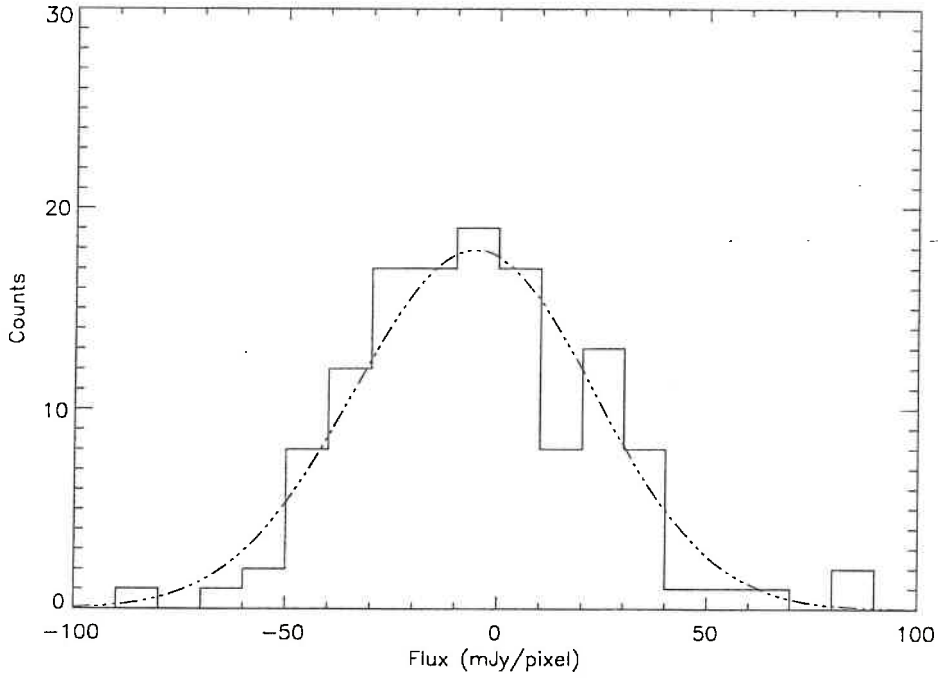

Figure 9: Statistics of pixels other than #5 at $\lambda = 60\mu$m. The parameters of the superimposed gaussian are $\bar{x}$ and σ_T given in table 5

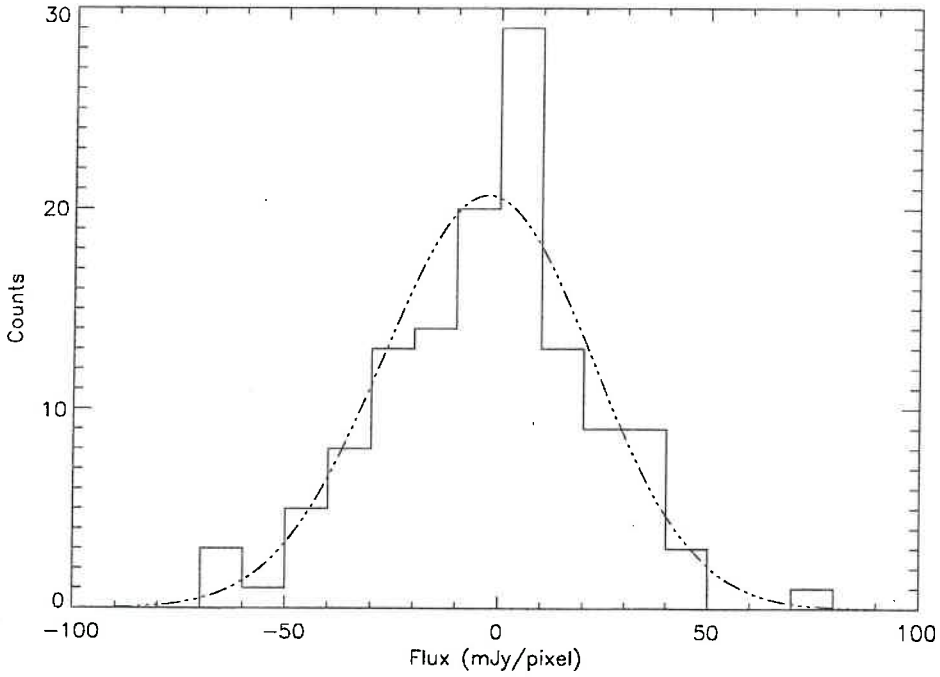

Figure 10: Statistics of pixels other than #5 at $\lambda = 90\mu$m. The parameters of the superimposed gaussian are $\bar{x}$ and σ_T given in table 5

λ	sources					
μm	3C284	1345+125	1819+39	1829+29	3C459	2352+49
60	99±41	957±41				
90		998±41	113±41	108±41		
160		860±120	310±120			
200		1530±280			890±280	1050±280

Table 4: Source flux (mJy) for "suspected" detections. Note that, as explained in the text source 1345+125 has wrong fluxes.

In that table are also given the average ON–OFF value ($\bar{x}$) and its error ($\sigma_{\bar{x}}$, computed as $\sigma_T/\sqrt{n}$, where n is the total number of pixel used, i.e. 8×number of sources). There might be a little offset from zero at 60μm. In this same table are also given σ, $\bar{x}$ and $\sigma_{\bar{x}}$ for pixel #5, which we shall discuss in sect. 3.2

For C200 (figures 11 and 12) the situation is less plane, at least for $\lambda = 200\mu$m. Remember that in this case we are examining the source fluxes (sect. 3.1). The values for σ_T, $\bar{x}$ and $\sigma_{\bar{x}}$ are given in table 7, after exclusion of source #24 and of a few other sources occurring in regions of very high background (and therefore with larger uncertainties). These data are referred to as "case 1". In "case 2" the same parameters have been computed after exclusion of a further few sources which might represent possible (2 sigma) individual detections. The purpose of this was to give a r.m.s. noise as close as possible to the actual noise (i.e. not contaminated by any signal). Table 7 shows that at 200μm there seems to be a significative offset, even after removal of "suspicious" sources: we do not believe this is an indication of a real average detection, but rather an inadequate correction of vignetting (see sect. 2.2).

3.2 Individual Detections

The comparison of the ON–OFF values of source #24 (1345+125) (pixel #5 for C100 and summ of the four pixels for C200) with σ_T shows that it is detected at a greater than 5 sigma level at all wavelengths. Unfortunately this source: *i*) is not a classical CSS since it has a Seyfert nucleus; *ii*) it was not properly scheduled for observations, therefore its flux turns out to be about a factor of two low with respect to IRAS.

For all the other sources, none is strong enough, with respect to the noise, to be safely detected. Possible 2–3 σ detections are 3C284 (#21), 1819+39 (#48), 1829+29 (#52), 3C459 (#60) and 2352+49 (#63), whose fluxes (computed as explained in sect. 1) are given in table 4. To slightly improve the S/N ratio, we averaged the values of the 60 and 90 μm and those of the 160 and 200 μm, since the two pair of wavelengths are quite close and a source giving signal in one filter is likely to give signal to the other as well. As expected the new σ_T decreases by $\sqrt{2}$ (see table 5 for the pair 60–90 μm, line marked with an #) and the five sources possibly detected at either frequency are confirmed, proving that their flux is unlikely to be due to a statistical fluctuation at one λ only.

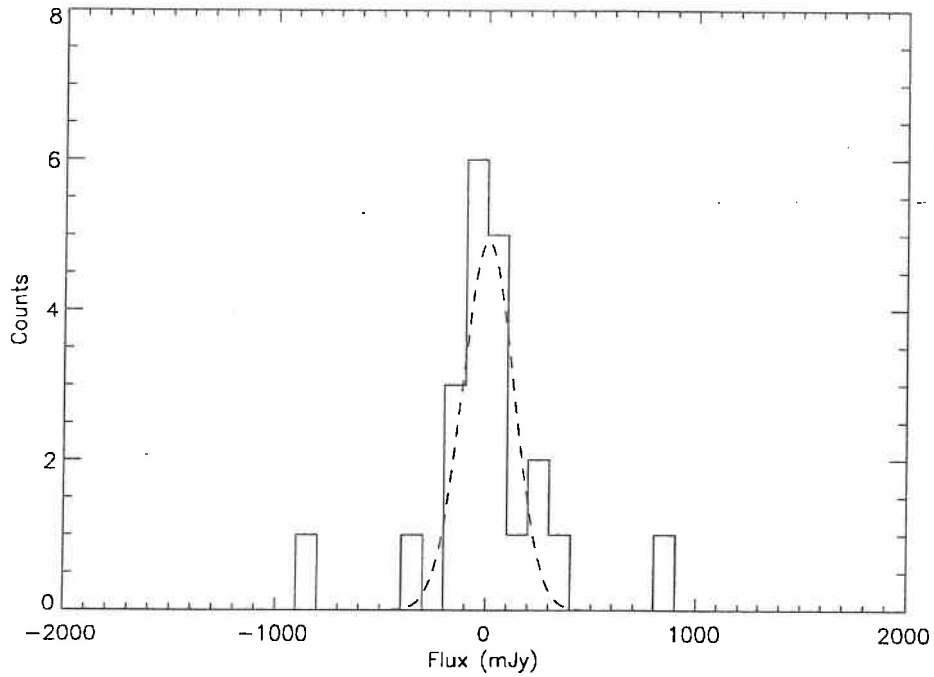

Figure 11: Flux statistics at $\lambda = 160\mu$m. The gaussian parameters are $\bar{x}$ and σ_T given in table 7 for "case" 2

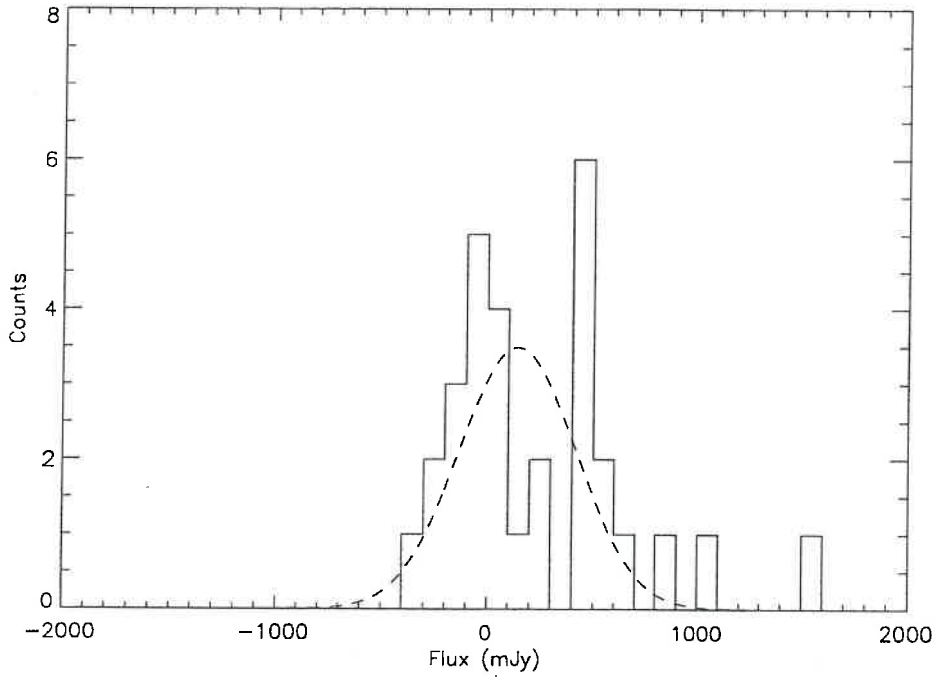

Figure 12: Flux statistics at $\lambda = 200\mu$m. The gaussian parameters are $\bar{x}$ and σ_T given in table 7 for "case" 2

3.3 Average Detections

Since no source except for 1345+125 is certainly detected, we have looked for an "average" emission from the sources of our sample (CSS and reference sources together).

In fig. 13 are plotted the histograms of the ON–OFF values for C100. Black bins refer to pixels #5 and white bins to the other pixels. Grey bins are those in which both pixels #5 and other pixels occur. Statistical tests (t–student and Kolmogorov–Smirnoff) prove that the two distributions are statistically different: at 60μm the probability that the differences are due statistical fluctuations are still about 10% ($\lesssim$ 2 sigma) but at 90μm this probability drops to $\leq$1% (almost 3 sigma).

We have then taken the average of all ON–OFF measurements on pixel #5, 1345+125 excluded. These values ($\bar{x}$) are reported in table 5, along with their standard deviation ($\sigma_{\bar{x}}$) computed as $\sigma_T\sqrt{n}$, where n is now the number of pixels #5, i.e. the number of sources considered. In the same table σ is the dispersion of pixels #5. The line marked with an # contains the average of the 60 & 90 μm values. While at 60μm the average value of pixel #5 differs from zero at only a 1.5 sigma level, (therefore we should, conservatively give an upper limit for an average detection of $3\times\sigma_{\bar{x}}$), at 90μm the average value is at about 3 sigma and can therefore be considered a real detection. This is reinforced by the averaged $(60+90)\mu$m values. In table 5 all fluxes are in mJy/pixel. The actual fluxes (mJy), i.e. corrected for f_{PSF} (see sect. 1) are given in table 6

For C200 the histograms of figures 11, 12 and table 7 do not allow us to state if any detection is present. We should, conservatively, put an upper limit to any average detection equals to $3\times\sigma_{\bar{x}}$ (case 2). The apparent positive detection at 200μm is most likely a systematic error not properly corrected yet, as discussed already in sec. 3.1

3.4 Comparison with IRAS data

In the works of Heckamnn et al (1992, 1994) one finds that the 3σ r.m.s. on individual measurements are $\approx$100 and $\approx$400 mJy at 60 and 100μm respectively, to be compared with $\approx$40mJy (σ_T/f_{PSF} from tables 5 and 2). Therefore, while at $\lambda = 60\mu$m ISO does not look much better (for the moment) than IRAS, at $\lambda = 90\mu$m the situation is markedly better.

The co–added values derived by Heckmann et al. 1994 for a sample of CSS/GPS radio galaxies are very uncertain. Considering their median values, that the authors themselves suggest as the more robust estimate, we deduce upper limits of $\approx$10 and $\approx$35mJy (1 sigma) at 60 and 100μm. These upper limits are in total agreement with ISO when considering the difference in redshift ($z = 0.45$ for our sample against $z = 0.76$ for theirs) which implies a reduction of $\approx$3 in their flux.

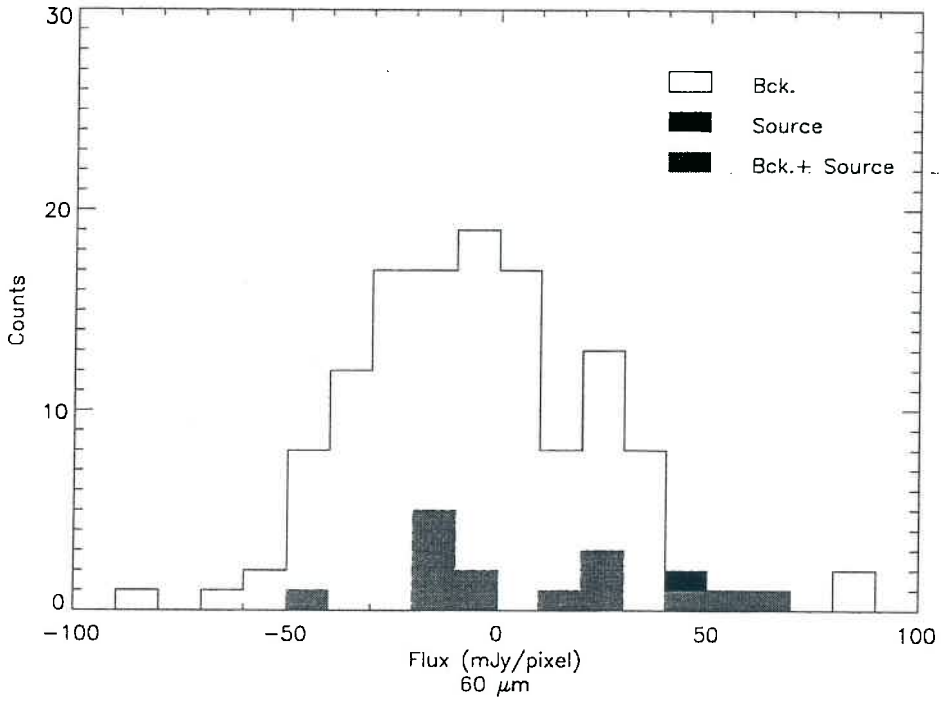

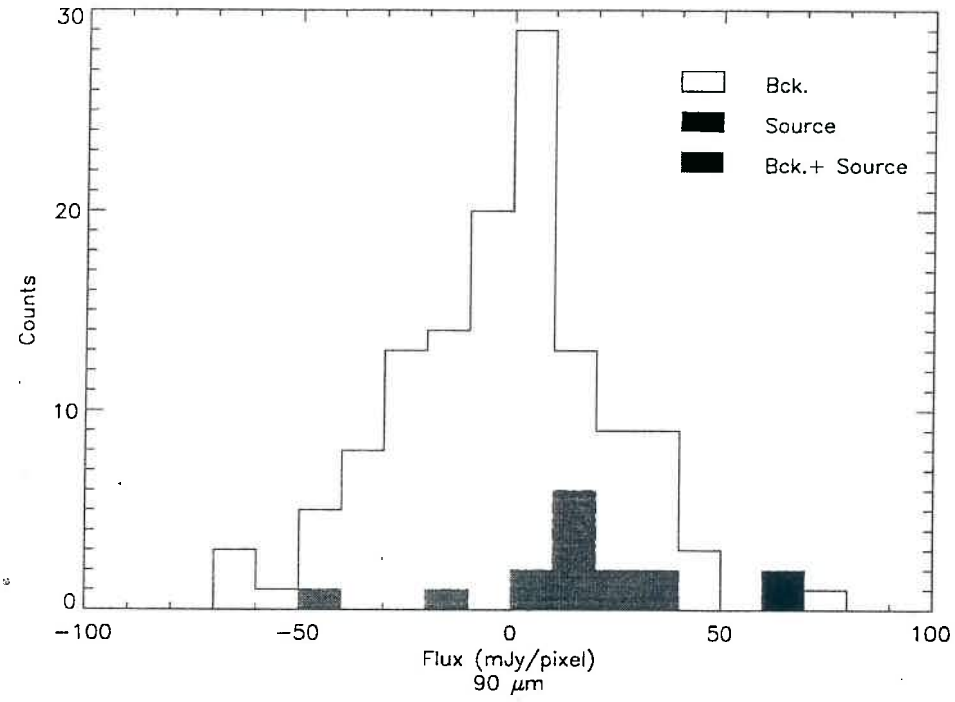

Figure 13: Hystograms of *pixels*=5 and of it pixels≠ 5). Source #24 excluded - [60μm missing]

λ μm	<*pixel* 5> mJy/pixel		<*other pixels* > mJy/pixel	
	$\bar{x} \pm \sigma_{\bar{x}}$	σ	$\bar{x} \pm \sigma_{\bar{x}}$	σ_T
60	11.1±7.1	31	-5.7±2.5	29
90	17.1±6.2	27	-2.7±2.2	25
#	14.1±4.9	24	-4.2±1.7	20

Table 5: Average flux values at $\lambda = 60$ and 90 μm. The line with an # gives the average of 60 & 90 μm values (see text). Source 24 excluded. Note that $\sigma_{\bar{x}}$ for pixel 5 is $\sigma_T/\sqrt{n}$

λ μm	<*pixel* 5> mJy
60	16±10
90	28±10

Table 6: Average flux values at $\lambda = 60$, 90 μm in mJy. Source #24 excluded

λ μm	case	S_{tot} mJy	
		$\bar{x} \pm \sigma_{\bar{x}}$	σ_T
160	case 1	26±35	140
	case 2	7±31	120
200	case 1	174±62	310
	case 2	144±56	280

Table 7: Average on all source flux values for $\lambda = 160$, 200 μm. At both wavelegths sources 11, 24, 52, 61 e 63 have been excluded because in high background regions. Source 48 at $\lambda = 160\mu$m and source 60 at $\lambda = 200\mu$ have been futher excluded (case 2) since possibly detected

	$\lambda = 60\ \mu$m	$\lambda = 90\ \mu$m	$\lambda = 160\ \mu$m	$\lambda = 200\ \mu$m
ISO data (mJy)	16 ± 10	28 ± 10	26 ± 35	174 ± 62
Expect. Synchrotron (mJy)	$1^{+0.6}_{-0.4}$	$1.6^{+1.0}_{-0.6}$	$2.4^{+2.6}_{-0.8}$	$3.4^{+0.7}_{-0.6}$

Table 8: ISO vs. expected synchrotron emission

	$\lambda = 60\ \mu$m		$\lambda = 90\ \mu$m		$\lambda = 160\ \mu$m		$\lambda = 200\ \mu$m	
	mean	median	mean	median	mean	median	mean	median
CSS	15 ± 13	-3^{+32}_{-19}	42 ± 13	23^{+11}_{-7}	84 ± 47	70^{+70}_{-70}	96 ± 94	50^{+20}_{-80}
S.RIF.	18 ± 17	-3^{+20}_{-14}	4 ± 17	16^{+3}_{-52}	-48 ± 53	-40^{+10}_{-40}	234 ± 83	200^{+80}_{-170}

Table 9: Mean and median fluxes (mJy) for CSS/GPS and comparison sample. Source #24 and high background sources (#s 11, 52, 61 e 63) excluded

4 Gas Mass

4.1 FIR tail of Synchrotron emission

For every source in the sample all the fluxes at radio wavelengths available in the literature have been collected and the spectrum properly fitted with a model which also includes a spectral curvature due to synchotron losses. From this spectrum the fluxes at 60, 90, 160 and 200 μm have then been extrapolated. Table 8 gives the median signal expected from synchrotron emission compared with the mean FIR signal measured by ISO.

Given the large errors of our measurements, we cannot draw any firm conclusion. Except for $\lambda = 90\mu$m, where the discrepancy between the two values is at an almost 3 sigma level, we can only conclude that the synchrotron emission is extremely low and cannot contribute too much to any FIR emission.

4.2 CSS/GPS and comparison sample

In table 9 are given the mean and median fluxes for CSS/GPS and for reference sources. From the mean we have excluded 1345+125 and, at long wavelengths, sources in high background regions. The statistics is still quite poor, but the values are totally compatible with each other. This means that the galaxies associated with CSS/GPS and those associated with extended radio sources do emit, on average, the same amount of FIR radiation. In other words, in the light of the present results, there is no reason to believe that CSS/GPS evolve in an unusual interstellar medium

4.3 Dust and Gas Mass

The (F)IR radiation due to heated dust in a galaxy, in the hypothesys the dust is transparent, follows a modified Planck law given by

$$S(\nu_0) = \frac{\mu(\nu_e) B_{c.n}(\nu_e) M_{dust}(1+z)}{D_L^2} \qquad (5)$$

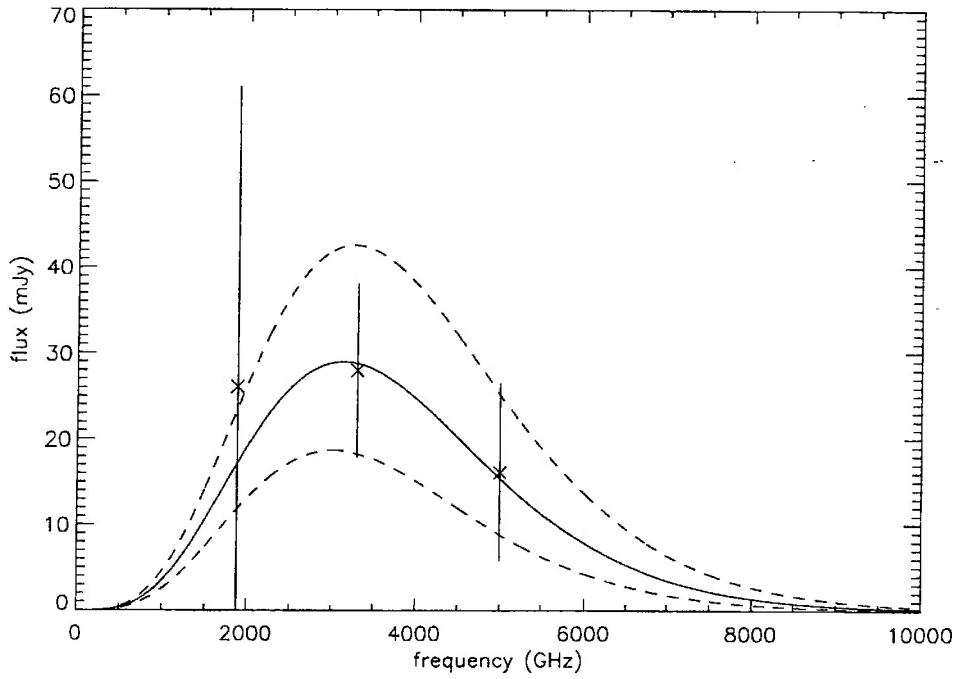

Figure 14: Best fitted curve from eq. 5. Dotted lines are obtained from the pairs of values: $[T-1\sigma, M_\odot - 1\sigma]$ and $[T+1\sigma, M_\odot + 1\sigma]$

where ν_o and ν_e are the observed and emission frequencies, μ the absorption coefficient, M_{dust} the dust mass, D_L the luminosity distance and z the source redshift. The absorption coefficient is usually assumed $\propto \nu^p$ with $p = 2$ for $\lambda > 20\mu$m. Adopting $\mu(\nu_e)$ =5.5 cm^{2}gr^{-1} at ν_e=1110 GHz (as in Chini and Krügel, 1994) we could fit eq. 5 to our average data (whole sample together) and estimate the dust mass and its temperature. We have excluded from the fit the value at 200μm since, as said already, we do not consider it reliable.

In spite of the large uncertanties in the average flux measurements the data seem to constrain the parameters reasonably well (see tables 10 and fig. 14). Chini and Krügel 1995 find in a sample of AGN's, $T = 33 \pm 5$ and $3 \times 10^5 M_\odot < M_{dust} < 5 \times 10^8 M_\odot$. Our values are not significantly different from these.

The dust temperature is not particularly low: we seem to be detecting a warm phase in these objects. Should the high value at 200μm turn out to be real, then we should begin to think to the presence of a further colder phase.

From the dust mass we can finally infer the gas mass, assuming a ratio between the two. In our Galaxy the ratio M_{gas}/M_{dust}=150 is usually assumed. Our galaxies are ellipticals and

M_{pol} $10^6 M_\odot$	T K	χ^2
2.3 ± 0.5	44 ± 2	0.08

Table 10: M_{pol} and T from the fit

at moderatly large redshift. Chini and Krügel, for objects with $z \sim 3$ adopt 500. With these values we would deduce $M_{gas} \approx (4 \div 10) \times 10^8 M_\odot$. From the theoretical models (e.g. de Young) or from the simplified model by Fanti et al. 1995, we find that to keep a normal source smaller than 15Kpc for its whole lifetime of 2×10^7years (frustrated source) a gas mass of $\approx (2 \div 6) \times 10^{10} M_\odot$ is required. In spite of all the uncertanties in our data such an amount of gas (and hence of dust) seems to have to be excluded.

The present conclusion is therefore that the warm dust we detect with ISO does not imply an amout of gas large enough to justify the frustration scenario of CSS/GPS radio sources.

5 Future observations

When we first looked at a bunch of data (6–8 sources) one year ago, the flux scale was quite different from now and the noise we evaluated at that time, although worse than expected, seemed to be acceptable for our purposes. This encouraged us to proceed, and to submit a new proposal for the second call to add a few more sources and try to improve the situation. We were granted 22Ksec, second priority. In addition H. Falcke, who had a program similar to ours, gave up to his observing time (5Ksec in second and 10Ksec in third priority) and, in agreement with the ISO team, this further time was given to us. So we totally revised our second observing schedule and planned longer observations on most of the sources.

At the end all sources will be observed (combining the two sets of data) four times what originally planned, or longer. Therefore the prelimirary results presented here will be, hopefully, improved.

Note however that for the long wavelengths, galactic and extragalactic confusion limits the individual detections (although it is reduced when co–adding the data) therefore there was no need to make extremely long observations, but just what required to push the noise below the above confusion limit.

Everybody can follow how the observations proceed by searching ISO homepage
(http://isowww.estec.esa.nl/)
then selecting:
SCHEDULE,
ISO Log,
Form to query the ISO Schedule,
ObserverID=CFANTI,
submit.
CSS_GPS refers to the original time allocation, CSS_GPS2 to the second one.

References

Chini R. and Krügel E., 1994, A&A, **288**, L33

Chini R. and Krügel E., 1995, ESO Messanger, **82**, 25

de Young D.S., 1993, ApJ, **402**, 95

Fanti C., Fanti R., Dallacasa D., Schilizzi R.T., Spenser R.E., Stanghellini C., 1995, A&A, **302**, 317

Fanti R., Fanti C., Schilizzi R.T., Rendong N., Parma P., van Breugel W.J.M., Venturi T., 1990, A&A, **231**, 333

Heckman T. M., O'Dea C.P., Baum S. A., Laurikainen E., 1994, ApJ, **428**, 65

Heckman T. M., Chambers K.C., Postman M., 1992, ApJ, **391**, 39

Table 11: Data corrected for *vignetting* and *flat-fielding* at λ=60 μm.

$\lambda = 60$ μm OFF, ON, ON–OFF									
source	*pixel* number								
	1	2	3	4	5	6	7	8	9
1	736	968	946	899	829	953	1008	984	955
R	727	947	957	915	844	926	955	981	934
	-27	-7	8	3	-15	-29	-35	-27	-19
7	1353	1278	1308	1359	1258	1290	1452	1448	1301
	1367	1276	1271	1430	1338	1274	1424	1437	1293
	3	-22	-12	23	27	-23	-24	-31	-26
11	1597	1567	1649	1692	1615	1564	1639	1709	1756
R	1632	1519	1621	1700	1677	1569	1644	1740	1715
	-37	-57	-18	-3	22	-7	-17	14	-85
19	943	967	942	973	900	972	845	890	841
R	922	896	961	975	938	961	834	872	846
	-10	-32	-12	-3	-11	-29	-22	-35	-39
21	743	666	692	666	723	686	701	733	713
R	776	652	661	704	810	692	714	729	740
	16	-24	-38	22	68	-8	-9	-10	7
22	616	484	589	548	577	726	659	572	621
	713	563	597	587	590	726	663	617	604
	88	82	5	24	-15	-10	-7	38	-31
24	894	865	960	898	979	905	884	963	1023
	964	1001	974	924	1777	945	874	985	1027
	27	81	14	54	660	33	-29	-7	-5
26	500	539	505	519	452	498	498	480	567
	534	533	501	514	487	508	460	516	555
	34	-9	-7	-11	26	4	-45	37	-14
30	621	500	540	500	639	520	474	509	580
	629	525	526	526	649	525	426	502	599
	-6	14	-25	21	-12	-3	-50	-22	10
34	558	510	579	541	637	546	545	568	534
	543	539	575	590	596	548	565	596	552
	-25	23	-13	37	-47	-4	20	21	5
48	655	585	532	564	600	576	546	508	572
	681	563	483	554	655	587	559	543	586
	28	-33	-47	-19	50	6	6	24	12
50	399	429	467	374	464	510	395	401	435
	406	395	427	404	478	521	413	378	441
	-1	-42	-44	26	-2	6	21	-22	-1

Table 12: cont.ed

$\lambda = 60$ μm OFF, ON, ON–OFF									
source	*pixel* number								
	1	2	3	4	5	6	7	8	9
52	663	684	656	678	750	726	730	686	659
	678	636	658	719	808	744	716	691	626
	8	-57	-1	33	47	17	-28	0	-45
58	716	622	552	625	631	631	581	632	567
R	712	614	604	610	644	647	626	605	596
	-17	-11	63	-18	-1	14	34	-41	22
59	517	599	561	603	598	550	606	600	571
R	568	576	540	598	617	573	572	659	585
	37	-39	-23	-16	11	23	-40	56	0
61	1102	919	857	888	751	549	855	1083	735
	1089	873	862	912	787	538	844	990	729
	-14	-46	1	19	42	-18	-17	-61	-3
63	531	598	632	620	551	616	612	590	543
	557	577	638	630	552	635	663	640	522
	-13	-28	6	5	-12	6	39	41	-32

Table 13: Data corrected for *vignetting* and *flat-fielding* at $\lambda = 90\mu$m.

$\lambda = 90$ μm OFF, ON, ON–OFF									
source	*pixel* number								
	1	2	3	4	5	6	7	8	9
1	645	700	691	697	646	662	710	731	691
R	646	698	707	668	652	675	673	740	697
	-1	-5	7	-30	10	9	-38	10	3
7	888	944	917	906	894	870	949	941	924
	891	947	914	925	874	885	921	979	900
	-2	0	-5	18	10	11	-29	36	-22
11	1136	1214	1232	1201	1167	1194	1191	1254	1233
R	1181	1209	1248	1168	1193	1207	1170	1233	1208
	33	-17	5	-2	12	6	-23	-25	-31
19	605	652	641	666	660	659	631	589	610
R	607	634	645	623	619	654	639	569	651
	3	-23	5	-48	-45	-2	5	-26	40

Table 14: cont.ed

$\lambda = 90\ \mu$m OFF, ON, ON–OFF									
source	*pixel* number								
	1	2	3	4	5	6	7	8	9
21	519	509	491	483	536	562	479	491	526
R	506	466	491	483	559	564	493	509	515
	-14	-44	-5	7	17	7	12	20	-17
22	431	392	403	399	384	401	384	387	391
	447	398	405	398	398	414	417	390	420
	13	10	8	-6	7	-2	45	1	22
24	655	652	667	608	610	614	640	705	686
	700	826	691	705	1216	682	674	699	677
	48	178	24	91	609	68	36	-6	-4
26	320	330	313	324	331	337	297	328	383
	329	334	298	355	337	341	329	336	369
	6	5	-17	32	7	14	33	1	-19
30	436	399	407	418	459	399	400	388	407
	456	401	437	387	491	431	342	423	483
	24	-10	32	-37	31	33	-64	32	72
34	459	439	447	449	441	443	439	450	461
	426	474	434	420	461	417	422	454	445
	-38	37	-15	-35	10	-21	-11	2	-19
48	428	382	410	407	453	381	381	383	390
	433	431	412	379	517	373	390	339	394
	-3	49	8	-27	69	-7	13	-46	4
50	380	390	388	348	389	420	384	372	404
	408	370	409	368	409	457	386	368	395
	8	-20	17	20	14	37	6	-14	-11
52	753	809	794	844	781	729	855	815	787
	707	800	791	790	847	726	812	808	763
	-47	-15	-8	-54	66	-6	-45	-6	-29
58	454	455	430	433	456	497	454	432	453
R	436	430	457	442	488	510	447	466	480
	-20	-37	27	8	37	2	-2	28	26
59	591	613	590	608	596	551	603	609	598
R	603	596	555	594	578	570	608	587	614
	11	-21	-32	-12	-16	19	2	-22	9
61	615	689	688	610	584	637	646	615	584
	626	716	649	614	608	570	582	594	576
	4	25	-38	-4	20	-64	-64	-21	-8
63	688	627	665	647	629	653	677	695	615
	711	632	666	657	659	668	692	684	626
	20	4	-2	7	24	15	17	-6	8

Table 15: Data corrected for *vignetting* and *flat-fielding* at $\lambda = 160$ μm.

$\lambda = 160$ μm OFF, ON, ON–OFF									
source	*pixel* number				source	*pixel* number			
	1	2	3	4		1	2	3	4
1	2555	2611	2585	2551	34	1617	1855	1773	1859
R	2504	2505	2575	2637		1586	1752	1772	1869
	-15	-103	-8	9		-37	-99	16	23
6	1810	1677	1763	1844	37	1106	1035	1036	1056
R	1777	1628	1758	1894	R	1073	1052	1069	1046
	-25	2	-9	57		-53	1	22	-15
7	3199	3142	3229	3269	41	927	1053	1026	987
	3157	3154	3237	3215		919	954	986	981
	-30	21	20	-41		-4	-94	-42	-10
11	4318	4659	4499	4200	48	1248	1197	1215	1310
R	4317	4504	4481	4388		1268	1410	1277	1357
	-2	-150	-19	184		10	199	60	41
17	892	885	1081	992	50	1776	1669	1541	1659
	1045	993	1062	933		1626	1688	1758	1674
	132	127	-21	-56		-156	3	171	3
19	1395	1353	1427	1339	52	5105	5027	4893	4951
R	1435	1337	1335	1389		4969	4565	4711	4831
	28	-29	-93	50		-126	-459	-175	-119
21	891	860	872	893	58	2475	2414	2381	2351
R	889	843	870	848	R	2483	2343	2408	2340
	0	-27	-23	-67		16	-63	36	-1
22	937	864	883	847	59	2879	2920	2911	2815
	983	912	928	928	R	2841	2841	2795	2912
	67	44	62	55		-42	-66	-111	106
24	2036	1982	1986	1947	61	5255	5502	5450	5412
	2176	2325	2196	2089		5078	5198	5519	5449
	145	355	215	149		-171	-321	75	35
26	943	1182	1249	1198	63	4844	4965	5114	4809
	1163	1147	1146	1225		4868	4847	5079	4924
	213	-59	-111	13		38	-86	-36	115
30	1386	1330	1377	1398					
	1375	1376	1392	1564					
	-21	87	-13	181					

Table 16: Data corrected for *vignetting* and *flat-fielding* at *lambda* = 200 μm.

$\lambda = 200$ μm OFF, ON, ON–OFF									
source	*pixel* number				source	*pixel* number			
	1	2	3	4		1	2	3	4
1	2931	3487	3278	3408	30	1846	1971	1866	1804
R	3162	3381	3401	3511		1748	1960	1970	2217
	255	-81	136	120		-58	-10	166	406
2	1587	1603	1376	1459	32	1347	1338	1241	1407
R	1734	1625	1389	1601		1363	1381	1177	1401
	206	59	26	139		28	59	-48	15
3	2105	1668	2043	1800	34	2549	2610	2771	2632
R	2310	1731	2126	1884		2554	2618	2705	2757
	188	111	88	85		-71	27	-16	141
5	2814	2443	2446	2321	36	1316	1168	1016	1050
R	3014	2336	2446	2411	R	1312	1118	1014	1011
	223	-104	-6	90		0	-46	-4	-37
6	2180	2359	2547	2445	37	1333	1292	1225	1292
R	2370	2234	2521	2494	R	1256	1239	1184	1191
	128	-189	53	162		-37	-80	19	-90
7	3908	3957	4091	4196	41	1524	1643	1697	1546
	4124	4146	4245	4198		1477	1483	1549	1482
	255	182	211	4		-22	-168	-81	-47
11	4940	5744	5555	5706	48	1431	1311	1406	1534
R	5525	5619	5858	5806		1339	1219	1322	1612
	452	-197	212	120		-62	-58	-62	97
17	1542	1562	2072	1696	50	1813	1949	1997	2088
	1474	1544	1971	1622		1726	1952	1990	2094
	-94	-65	-81	7		-109	48	11	25
19	1577	1515	1673	1635	52	5610	6043	5871	6690
R	1475	1467	1603	1676		5559	6680	5910	6432
	-109	-37	-51	56		-76	301	-139	-321
21	1959	1721	1636	1584	56	2577	2393	2100	2841
R	1988	1688	1670	1656		2670	2317	2067	2859
	69	3	35	109		95	-63	-31	34
22	2271	1989	1877	1713	58	3213	3305	3251	3360
	2280	2027	2019	1968	R	3427	3259	3429	3377
	7	108	97	230		240	-31	230	39

Table 17: cont.ed

$\lambda = 200\ \mu$m OFF, ON, ON–OFF									
source	*pixel* number				source	*pixel* number			
	1	2	3	4		1	2	3	4
24	2409	2481	2602	2483	59	3497	3818	3626	3645
	2888	2856	2981	2788	R	3738	3698	3642	3822
	446	383	375	321		279	-111	55	203
26	1688	2205	2306	2000	60	2872	2027	1703	1754
	1951	1989	1808	2111	R	2981	1986	2020	2142
	322	-170	-374	173		151	3	343	391
28	1349	972	1203	1074	61	6926	7804	6058	7534
R	1313	941	1180	1034		6651	6212	7261	7774
	-7	-55	-6	-8		23	-844	328	340
29	813	805	676	561	63	5917	5579	6666	6395
R	938	697	683	581		6355	6575	6706	6758
	134	-91	5	27		349	419	-38	323